Impacts of Anthropogenic Heat Flux and Urban Land-Use Change on Frontal Rainfall near Coastal Regions: A Case Study of a Rainstorm over the Pearl River Delta, South China

JUNPENG WEN,[a,b,c] JI CHEN,[b] WENSHI LIN,[a,d,e,h] BAOLIN JIANG,[a] SUISHAN XU,[f] AND JING LAN[g]

[a] *School of Atmospheric Sciences, Sun Yat-sen University, Guangzhou, China*
[b] *Department of Civil Engineering, University of Hong Kong, Pokfulam, Hong Kong, China*
[c] *Meteorological Center of Central South Regional Air Traffic Management Bureau of Civil Aviation Administration of China, Guangzhou, China*
[d] *Key Laboratory of Tropical Atmosphere-Ocean System, Sun Yat-sen University, Ministry of Education, Zhuhai, China*
[e] *Southern Marine Science and Engineering Guangdong Laboratory (Zhuhai), Zhuhai, China*
[f] *Haizhu District Meteorological Observatory of Guangzhou, Guangzhou, China*
[g] *Guangzhou Climate and Agrometeorology Center, Guangzhou, China*

(Manuscript received 16 November 2018, in final form 28 December 2019)

ABSTRACT

This study investigated heavy frontal rainfall that occurred on 13–14 October 2011 over the Pearl River Delta (PRD) in China. The frontal rainstorm was simulated using the WRF-ARW Model (version 3.3), which included its urban canopy model. Although the model-simulated convection occurred 2 h early and the second precipitation peak was underestimated, the model represented the formation, development, and extinction of the frontal rainfall and captured the distribution of the peak value. In addition, the averaged value of 49.7 W m^{-2} was taken as the anthropogenic heat flux (AHF) of the PRD, and two land-use datasets were adopted: one for 1992 and the other for 2011. The simulation revealed that AHF and urban land-use change (ULUC) increased the total rainfall over the PRD by 6.3% and 7.4% and increased the maximum hourly rainfall intensity by 24.6% and 21.2%, respectively. Furthermore, to elucidate the mechanism of AHF and ULUC influence, the rainstorm structure, low-level jet (LLJ), and CAPE of the rainfall event were analyzed. It was found that AHF and ULUC enhanced two strong southward LLJs located over the urban areas, which carried abundant water vapor to the PRD and generated additional upper-level CAPE. This not only sustained steady ascent of the air, but it also created conditions favorable for downward motion, resulting in large persistent convective clouds and heavy frontal rainfall.

1. Introduction

Human activities can cause land-use change and release anthropogenic heat to the atmosphere. Urbanization refers to the process of increase of the urban population and expansion of urban land use. Urbanization can notably modify local and even regional meteorological variables—for example, temperature, wind speed, humidity, and PBL height—and can affect the exchange of surface energy between the land surface and the atmosphere (Nemunaitis-Berry et al. 2017; Gutiérrez et al. 2015; Dou et al. 2015). Some previous studies explored the influence of urbanization on urban climate processes (Jin et al. 2005), UHIs (Chen and Zhang 2018), contributions of urban environments to global warming (Parker 2004, 2006), changes of precipitation (Kaufmann et al. 2007; Schmid and Niyogi 2017), and reduced air moisture and evaporation in cities (Yang et al. 2017). With the increase in built-up areas and intensification of human activities over the past several decades, urbanization has induced significant modifications of regional atmospheric circulations that can result in more intense rainfall (e.g., Alexander et al. 2006; Allan and Soden 2008). Researchers have used observational data to study the temporal and spatial variability between urbanization and precipitation (Hand and Shepherd 2009; Shepherd et al. 2002). Using high-resolution radar

[h] ORCID: 0000-0002-5767-0051.

Corresponding author: Wenshi Lin, linwenshi@mail.sysu.edu.cn

Publisher's Note: This article was updated on 9 March 2020 to correct the format of the author affiliation denoted by the footnote d.

DOI: 10.1175/JAMC-D-18-0296.1

reflectivity and lightning data in the southeast United States, Ashley et al. (2012) illustrated that demographic and land-use changes feed back to local atmospheric processes that promote thunderstorm formation and persistence. Grum et al. (2006) reported a clear tendency that extreme precipitation events affecting urban drainage and causing flooding will become more frequent as a result of climate change.

With the rapid development of numerical models, more and more researchers used numerical simulation to reveal the relationship between urbanization and the emergence and development of storms. Employing the WRF Model, Shem and Shepherd (2009) showed that rainfall amounts downwind of Atlanta, Georgia, could be 10%–13% higher within a strip 20–50 km east of the city when land use changed from dry land, cropland, and pasture to urban land cover. Using a 2-km-resolution WRF Model, Meng et al. (2012) indicated that the UHI of the city of Guangzhou in the Pearl River Delta (PRD) in South China and the dry island effect produced by the land surface could lead to a convergence zone with enhanced CAPE. In a study of four events of summertime rainfall in Beijing, China, Nie et al. (2017) found that anthropogenic heat increased sensible heat flux, enhanced mixing and turbulent energy transport, lifted PBL height, increased dry static energy, and destabilized the atmosphere in urban areas, which resulting in enhanced convergence during the major rainfall period. At the same time, some other studies have come to the opposite conclusion. Zhang et al. (2009) found that urban expansion can produce less evaporation, more mixing of water vapor in the boundary layer, and therefore less convective available potential energy and more convective inhibition energy. The combination of these factors induced by expanding urban surfaces was helpful in reducing precipitation for the Beijing area. Similarly, using the fifth-generation Pennsylvania State University–National Center for Atmospheric (NCAR) Research Mesoscale Model (MM5), Guo et al. (2006) found that the decrease of total accumulated precipitation in the urbanized areas was mainly due to the effect of the decreases cloud peak updraft and the intensified downdraft. Therefore, it can be inferred that urbanization play a direct role in the initiation and development of convection. However, rainfall processes are complicated and the understanding of the influence of urbanization on such processes, especially frontal rainfall processes, remains limited, meaning further explorations are necessary. To this end, this study focused on investigation of the influence of AHF and urban land-use change (ULUC) on frontal rainfall using the WRF Model.

The study area was the PRD region. Rapid economic development over the previous 30 years has meant this region has experienced considerable urbanization, making it an ideal testbed to explore the influence of urbanization on rainfall. Chen et al. (2011) revealed that the urbanization effect in the study area since 1984 has caused an increasing trend in daily minimum surface temperature with a rate of about 0.6°C per decade; correspondingly, they found decreasing trends in relative humidity in two cities in the PRD, that is, Guangzhou and Shenzhen. Lin et al. (2007, 2009) employed a regional climate model (i.e., the MM5) to simulate the impact of urban expansion in the PRD region using two different land covers. They found that urbanization results in increased monthly mean air temperature and sensible heat flux (SHF) and decreased diurnal temperature range, relative humidity, atmospheric water vapor, and latent heat flux (LHF). To further confirm and improve our understanding of the influence of urbanization on rainfall over the PRD region, this study considered a heavy frontal rainstorm as a case study.

The remainder of this paper is structured as follows. Section 2 introduces the data used and the model setup, and section 3 describes the synoptic environment of the case study. Section 4 presents validation of the model simulation, and section 5 provides the study results. The paper ends with the presentation of our conclusions in section 6.

2. Research data and model setup

The research data used in this study included rainfall data at 1-h intervals and near-surface meteorological data at 3-h intervals, which consisted of air temperature and dewpoint temperature at 2 m above the ground, sea level pressure, and wind speed and wind direction at 10 m above the ground. These data were derived from the Meteorological Information Comprehensive Analysis and Processing System created by the China Meteorological Administration, and this study used data recorded at more than 4000 automatic weather stations in South China.

This study adopted the WRF-ARW Model, version 3.3 (Skamarock et al. 2008), which is a nonhydrostatic, fully compressible, primitive equation model, to simulate the frontal rainstorm. The effort to develop the WRF Model has been a collaborative partnership, principally among the NCAR, National Atmospheric and Oceanic Administration, National Centers for Environmental Prediction (NCEP), and other governmental agencies in the United States. In this study, the WRF Model used a threefold one-way nesting system, 31 vertical levels, and a nesting system that included three model domains with three spatial resolutions of 27, 9, and 3 km (Fig. 1a). The initial and boundary conditions for the model were interpolated from the NCEP Global Final reanalysis dataset, which has 1° × 1° spatial resolution and 6-h temporal

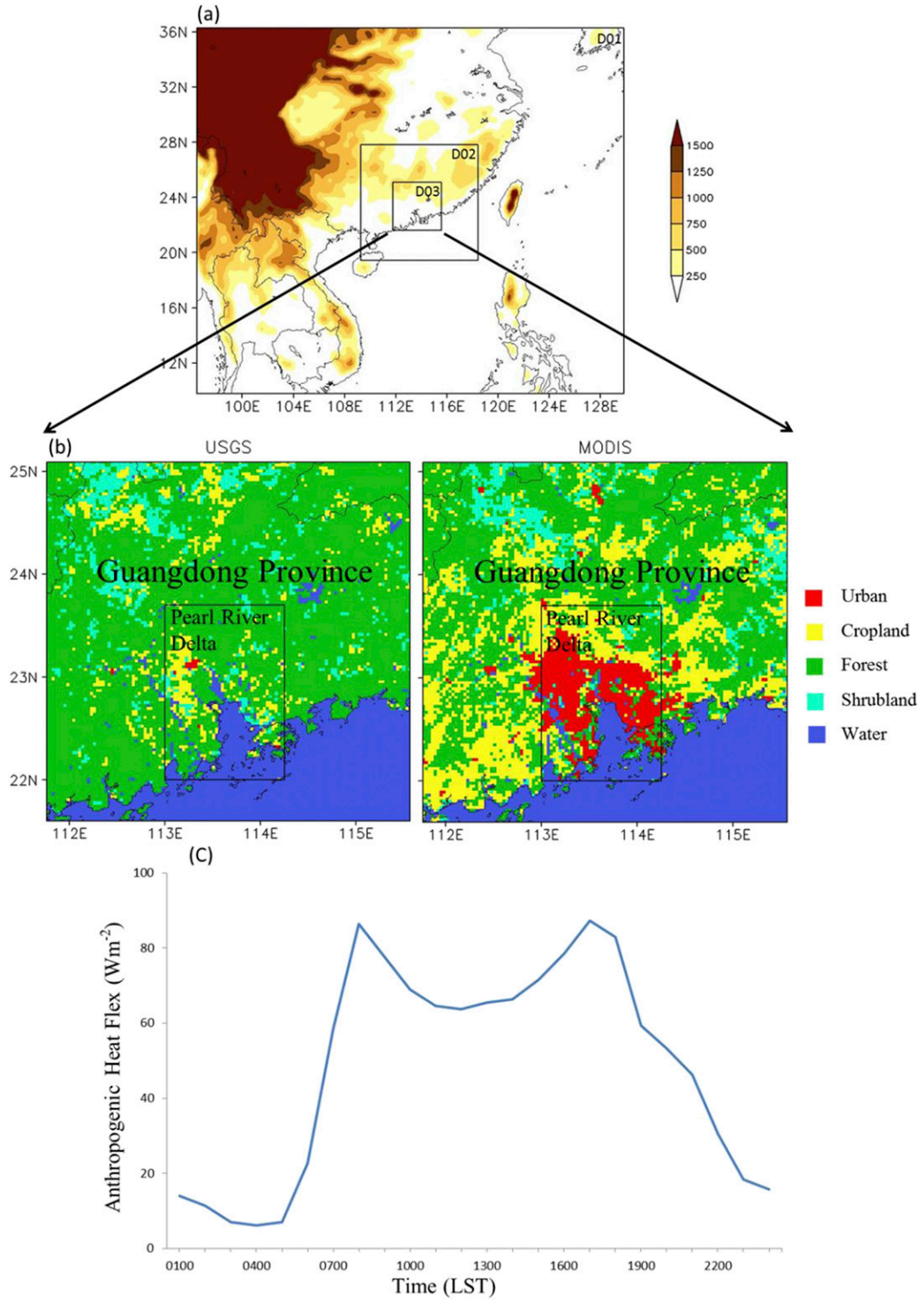

FIG. 1. (a) Domains and terrain elevation (shading; m) used for the WRF-ARW simulation, (b) D03 land use of USGS and MODIS with 3 × 3 km resolution, and (c) hourly anthropogenic urban heat flux ($W m^{-2}$) in 2011.

TABLE 1. Anthropogenic heat flux.

	Increasing rate of power consumption (%)	Change in rate of car ownership (%)	Change in rate of AHF (%)	Avg AHF ($W m^{-2}$)	AHF peak ($W m^{-2}$)
2009	—	—	—	41.1	73.2
2010	12.5	8.12	11.77	45.9	80.8
2011	8.35	6.80	8.09	49.7	87.3

resolution. The model simulation duration for all three domains was from 0800 local standard time (LST) (in this study, LST = coordinated universal time + 8 h) 13 October 2011 to 0800 LST 14 October 2011 (i.e., a 24-h period).

Certain schemes were selected in the WRF-ARW Model to simulate some physical processes of the atmosphere. This study focused on the application of the microphysics and cumulus schemes (Wang and Seaman 1997; Giorgi and Shields 1999). Thus, the WRF single-moment 6-class microphysics scheme (Hong and Lim 2006) was selected for the gridscale cloud and precipitation processes because this scheme has performed successfully for some heavy rainfall simulations (e.g., Choi et al. 2011; James et al. 2011; Shin and Hong 2009). Cumulus schemes are responsible for the subgrid-scale effects of convective and shallow clouds. In general, cumulus parameterizations should not be used in a grid with less than 5-km resolution when the model can resolve the convective eddies itself (Skamarock et al. 2008). Therefore, in this study, the Grell-3 cumulus parameterization (Grell and Devenyi 2002) was used for the first and second domains, and the no-cumulus parameterization was selected for the third domain. This study selected the Yonsei University scheme for simulating the PBL (Hong and Pan 1996) and the Noah land surface model (Chen and Dudhia 2001) for simulating terrestrial physical processes. In addition, for radiation processes, this study employed the RRTM for longwave radiation (Mlawer et al. 1997) and simple shortwave radiation (Dudhia 1989).

For the third domain only (i.e., the inner domain, D03), we applied the urban canopy model (UCM) to simulate the influence of urbanization. The UCM is a single-layer model for simplifying urban geometry. Some of the features of the UCM include shadowing from buildings, reflection of shortwave and longwave radiation, the wind profile in the canopy layer, and a multilayer heat transfer equation for roof, wall, and road surfaces (Kusaka et al. 2001; Kusaka and Kimura 2004).

To evaluate the impacts of ULUC on the PRD (Fig. 1b), this study used two land-use datasets. One dataset comprised original USGS 24-category land-cover data for the 12-month period from April 1992 to March 1993, and the other dataset was derived from current MODIS satellite imagery with 500-m spatial resolution. Comparison of the USGS and MODIS land-use data revealed substantial increase of the urban areas in midsouthern Guangdong, (i.e., the PRD region) within the region 22.00°–23.70°N, 113.00°–114.25°E.

To explore the influence of AHF on rainfall, this study estimated the AHF value for the PRD. Some previous studies have analyzed the diurnal AHF range (e.g., Sailor and Lu 2004; Lin et al. 2008) and they found that the average AHF emissions in large cities are mostly within 5–60 $W m^{-2}$ (Allen et al. 2011). Taking into account the different sources of AHF, for example, factories, vehicles, and residents, Wang and Wang (2011) estimated the average value of AHF in Guangzhou in 2009 was 41.1 $W m^{-2}$. In accordance with the methodologies described in both Sailor and Lu (2004) and Sailor and Hart (2006), this study used an AHF diurnal variation curve from the National Urban Database and Access Portal Tool (Ching et al. 2009). Furthermore, using a weighted average algorithm (Wang and Wang 2011) for the increased rates of power consumption and car ownership (see Table 1) from 2009 to 2011, this study assigned the daily averaged AHF as 49.7 $W m^{-2}$ and the dual-peak AHF value at 0800 and 1700 LST as 87.3 $W m^{-2}$ (Fig. 1c).

Given the above model setup, this study further designed three experiments to explore the impacts of urbanization on the case study frontal heavy rainstorm. We designed a control test (hereinafter CTL), which used the MODIS land-cover data and the above assigned AHF values, and an experiment using the MODIS data without AHF (hereinafter MOD). Through comparison of the CTL and MOD experiments, we explored the sensitivity of the simulation of this heavy rainstorm event to the treatment of AHF. Then, with the third experiment (hereinafter USG), which used the USGS land-cover data without AHF, we investigated the response of precipitation with respect to ULUC through comparison with the MOD experiment. In addition, the effect of AHF associated with ULUC on the frontal rainfall was examined through comparison of the CTL and USG experiments.

3. Synoptic environment of the case study rainstorm

To understand the mechanism of the heavy frontal rainstorm over the PRD that started on 13 October 2011, we first analyzed the related synoptic atmospheric

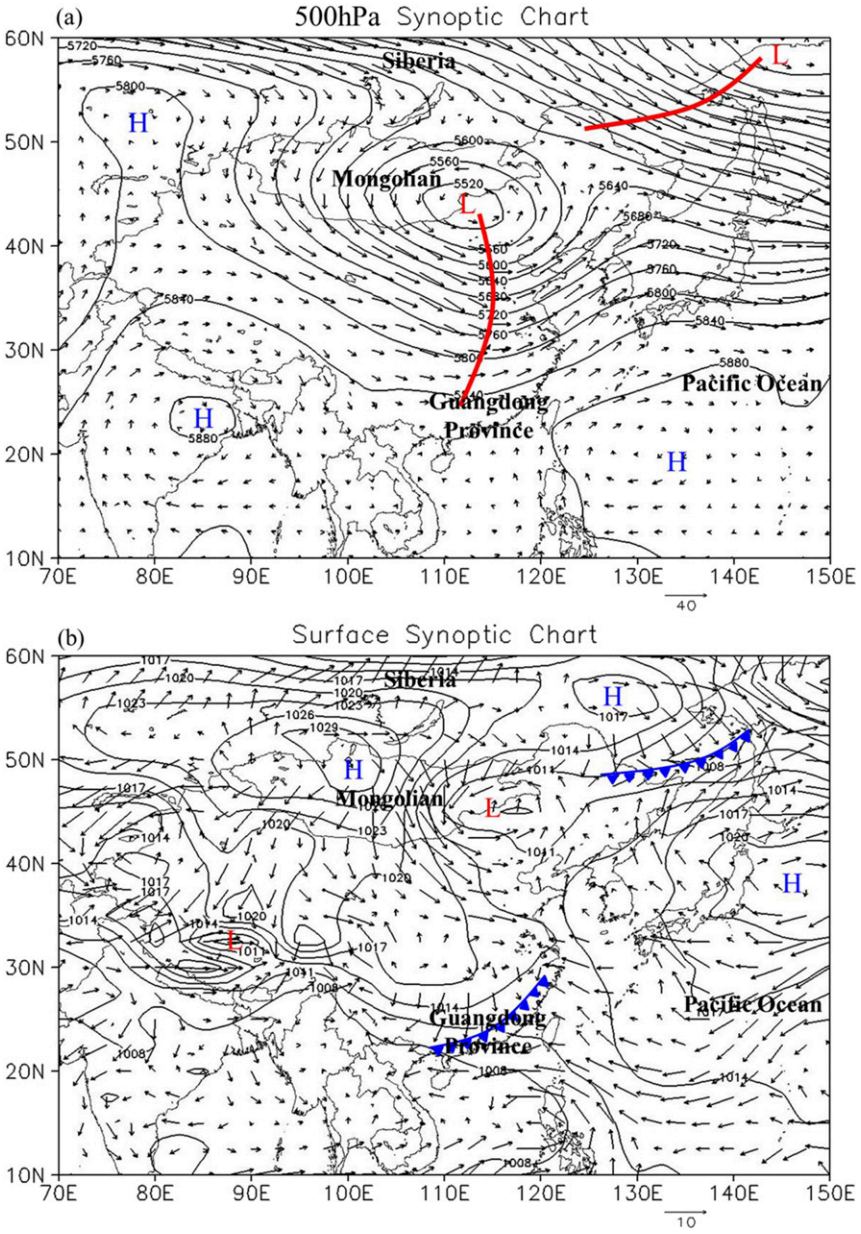

FIG. 2. Synoptic charts at 2000 LST 13 Oct 2011 obtained from the NCEP–NCAR reanalysis (2.5° × 2.5°): (a) 500-hPa geopotential height (isolines; m), and (b) sea level pressure (isobars; hPa) and wind vectors (m s^{-1}), showing troughs of low pressure (red solid lines) and ridges of high pressure (blue H symbols) in (a) and cold fronts over Eurasia in (b).

conditions. Figure 2a shows the 500-hPa geopotential height obtained from the NCEP–NCAR reanalysis data (2.5° × 2.5°) over Eurasia at 2000 LST 13 October 2011, that is, when the rainfall commenced. Before the rainfall started, it can be seen that a deep area of low pressure developed over the midlatitude region of northeastern China. In addition, subtropical areas of the western Pacific Ocean were dominated by an extensive area of high pressure at 500 hPa, namely, the western Pacific subtropical high. As the deep low pressure over northeastern China developed steadily and moved southeastward, it combined with a westerly trough extending from Mongolia to southern China, which affected much of South China at 2000 LST 13 October 2011. Under the influence of the western Pacific subtropical high, a southerly airflow appeared toward the northern side along the isobaric line, which provided the macroscale circulation for the heavy rainstorm (Fig. 2a).

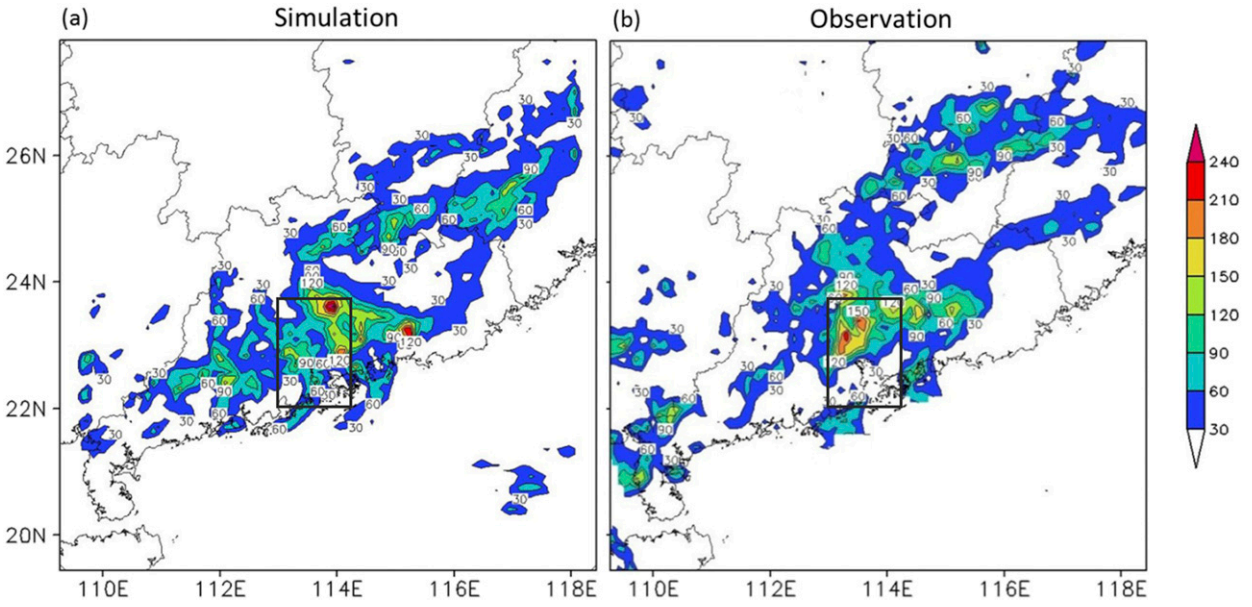

FIG. 3. (a) Simulated and (b) observed accumulated precipitation (shading; mm) from 0800 LST 13 Oct to 0800 LST 14 Oct 2011. Observed data were obtained by interpolating precipitation data from Guangdong Meteorological Observatory [Meteorological Information Comprehensive Analysis and Processing System (MICAPS)] using the Cressman interpolation technique (Daley 1991).

Consistent with the mid–upper-atmospheric situation, a strong area of high pressure was located over Siberia (Fig. 2b). A strong northerly surface wind dominated North China, and a cold front moved from the northwest toward the southeast, which affected Guangdong Province at 2000 LST 13 October 2011. Furthermore, abundant water vapor accumulated over Guangdong Province because a cold dry northwesterly wind from the Mongolian Plateau met with a warm moist southeasterly wind from the western Pacific Ocean. This vertical synoptic structure with a warm wet inflow at the lower level and cold dry air at mid–upper levels provided unstable conditions beneficial for a convective system, which caused the heavy rainstorm event.

4. Model simulation

Using the WRF-ARW Model and the research data detailed above, this study simulated the process of the case study rainstorm. To examine the detail of the frontal rainfall, we analyzed the amount and distribution of 24-h accumulated precipitation. Figure 3a shows the simulated 24-h accumulated precipitation (mm) over the second domain (denoted D02) (see Fig. 1a) from 0800 LST 13 October 2011 to 0800 LST 14 October 2011. Figure 3b shows the 24-h accumulated observed precipitation for the study period. The observed precipitation shows the rainband aligned from southwest to northeast, matching the orientation of the cold front (Fig. 2b). Comparison of the simulated and observed accumulated precipitation reveals the simulation captured the rainband satisfactorily. The observed precipitation occurred in the central region of the PRD and the maximum amount of accumulated precipitation was 319.8 mm. The averaged accumulated precipitation amount derived from stations in the d02 region was 35.9 mm. According to the historical records of the Guangdong Province Meteorological Observatory, this heavy rainstorm was the most severe precipitation episode in this area since 1951. The maximum precipitation of the simulation was 278.3 mm and the center of the distribution of heavy precipitation was located over the PRD, in agreement with the observations.

To further evaluate the performance of the simulations, Table 2 lists the statistical results of the simulated rainstorm over domain D03. These statistical results include the mean bias (MB):

$$\mathrm{MB} = \frac{1}{MN}\sum_{j=1}^{M}\sum_{k=1}^{N}(C_{j,k}^{m} - C_{j,k}^{o}),$$

mean absolute gross error (MAGE):

$$\mathrm{MAGE} = \frac{1}{MN}\sum_{j=1}^{M}\sum_{k=1}^{N}|C_{j,k}^{m} - C_{j,k}^{o}|,$$

root-mean-square error (RMSE):

$$\mathrm{RMSE} = \frac{1}{M}\sum_{j=1}^{M}\sqrt{\frac{1}{N}\sum_{k=1}^{N}(C_{j,k}^{m} - C_{j,k}^{o})^{2}},$$

TABLE 2. D03 averaged performance statistics of observed data and WRF predictions from 0800 LST 13 Oct to 0800 LST 14 Oct 2011.

Variable	Data	Avg	MB	MAGE	RMSE	FAE (%)	R
T2 (°C)	Obs	23.28	−0.26	0.48	0.54	2.12	0.98
	CTL	22.92					
Td2 (°C)	Obs	22.07	−0.54	0.57	0.73	2.72	0.96
	CTL	21.53					
SLP (hPa)	Obs	1011.19	0.15	0.76	1.01	0.08	0.49
	CTL	1011.34					
WS10 ($m\,s^{-1}$)	Obs	2.06	1.17	1.14	1.26	41.03	0.67
	CTL	3.23					
WD10 (°)	Obs	154.67	−47.86	41.47	52.82	29.18	−0.18
	CTL	116.78					

fractional absolute error (FAE):

$$\mathrm{FAE} = \frac{1}{MN}\sum_{j=1}^{M}\sum_{k=1}^{N}\frac{|C_{j,k}^{m} - C_{j,k}^{o}|}{(C_{j,k}^{m} + C_{j,k}^{o})/2},$$

and correlation coefficient R, where C^m and C^o are values of model prediction and observation, respectively; M is the number of stations; and N is the number of hour series. From Table 2, it can be seen that the diurnal variation of surface (2 m) temperature T2, dewpoint temperature at 2 m Td2, and sea level pressure (SLP) were estimated very well, with values of R reaching 0.99, 0.98, and 0.83, respectively. However, a cold bias of up to −0.49°C was found in T2, and the associated values of MAGE, RMSE, and FAE were 0.50°C, 0.54°C, and 2.20%, respectively. It is known that other meteorological models produce MBs from −0.20° to −0.91°C for surface temperature—for example, MM5 (Gilliam et al. 2006; Chen et al. 2009), which are likely due to limitations in the PBL scheme, LSM, and radiation schemes. Although the overprediction in Td2, with MB of up to −0.63°C, RMSE of 0.74, and FAE of 3.02%, indicates small underprediction in humidity, good correlation was found between the simulation and the observations, with the value of R reaching 0.98. At the same time, the values of MB, FAE, and RMSE with respect to SLP were 0.24°C, 0.06%, and 0.75, respectively, indicating good overall agreement between the observations and the simulation. Moderate overprediction (MB = 1.46 $m\,s^{-1}$) for wind speed at 10 m WS10 and large underprediction (MB = −47.86°) for wind direction at 10 m WD10 were found over domain D03. A high bias of surface wind speed over land has been found in every version of the WRF Model, caused by unresolved topographic features (Cheng and Steenburgh 2005; Rontu 2006). As the surface wind speed was overestimated, the simulation indicated the cold front dominated the PRD earlier than observed,

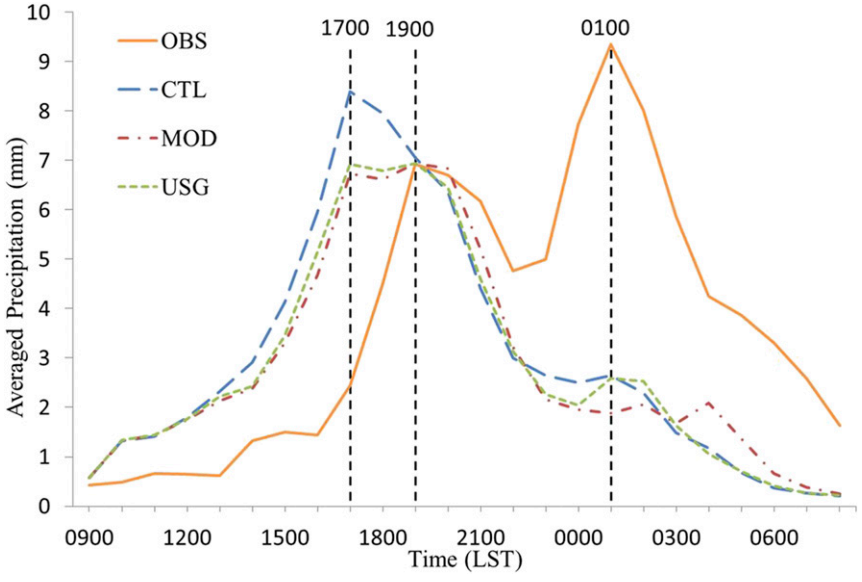

FIG. 4. Hourly area-averaged precipitation (mm) of observed data and WRF predictions in PRD from 0800 LST 13 Oct to 0800 LST 14 Oct 2011.

which led to the significant differences in angle between the modeled and observed wind directions.

Furthermore, the simulated precipitation failed in presenting the second peak of precipitation in the PRD at 0100 LST 14 October 2011 (Fig. 4). However, the occurrence of the center and the maximum precipitation of this frontal rainfall over the PRD (Fig. 4) between 1500 LST 13 October 2011 and 0000 LST 14 October 2011 was captured by the CTL between 1300 LST 13 October 2011 and 2200 LST 13 October 2011. Comparison of the time series of hourly area-averaged observed precipitation with the three experiments revealed the tendency of the curve for the CTL was closest to the observations. Because of the inclusion of AHF and ULUC, the CTL showed a pattern similar to the observations during the first major rainfall period and it presented the significant first peak of precipitation at 1700 LST 13 October 2011. In contrast, both the MOD and the USG failed to present the first precipitation peak and they moderately underestimated the total amount of precipitation. The observed area-averaged 24-h accumulated precipitation in the PRD area was 90.26 mm (not shown), whereas the precipitation simulated by the three experiments was 71.89, 67.63, and 66.91 mm (Table 3). As incorporation of AHF and ULUC in the simulation produced a pattern similar to the observations, we note that the use of AHF and ULUC in this study was rational, objective, and necessary. However, in terms of peak precipitation, the simulated rainfall was initiated two hours earlier than observed. Similar bias was found by Wan and Xu (2011) in their study of the third most severe flood event in Guangdong Province from 1950 to 2010. Overall, the simulation results were reasonably consistent with the actual situation, representing the formation, development, and extinction of the frontal rainfall, even though the simulated peak precipitation occurred two hours earlier than observed.

Water vapor transport is one of the most important mechanisms in relation to frontal rainfall. To investigate the development of the heavy rainfall of the case study, the time evolution of the water vapor mixing ratio at 850 hPa and radar reflectivity at the height of 3 km were analyzed. Figure 5 shows the simulated 850-hPa water vapor mixing ratio and wind. It also shows that the simulated radar reflectivity matches well with that observed in the PRD. The rainfall commenced over the northern PRD at 1000 LST 13 October 2011 when there was a sufficient band of water vapor (more than 13 g kg^{-1}) across Guangdong Province (Fig. 5a). At that time, Fujian, Hunan, and Jiangxi Provinces were already affected by the cold northerly winds, whereas

TABLE 3. Simulated 24-h accumulated precipitation in PRD from 0800 LST 13 Oct to 0800 LST 14 Oct 2011.

Test	PRD accumulated precipitation (mm)	Increasing accumulated precipitation in PRD (mm)	Increasing rate of accumulated precipitation in PRD (%)
CTL	71.89	—	—
MOD	67.63	4.26	6.30
USG	66.91	4.98	7.44

Guangdong Province was dominated by a warm southeasterly flow. By 1400 LST 13 October 2011, as the upper trough strengthened and the surface cold air advanced, the band of water vapor moved farther southward (Fig. 5d). A convective cell formed and developed at the center of the water vapor maximum over the PRD, which provided meteorological conditions beneficial for the heavy rainfall indicated by the radar reflectivity (Fig. 5e). At 1800 LST 13 October 2011, the convective cells located over the PRD corresponded to a shear line aligned from the southwest toward the northeast and a decreasing water vapor mixing ratio (Fig. 5g), which produced the heavy rainfall in the urban areas that was indicated by the strong radar reflectivity (56.12 dBZ). The water vapor band moved farther southeastward as the cold front strengthened with increasing northerly winds and a decreasing water vapor mixing ratio (Fig. 5j). Because of the overprediction of wind in the model, the cloud moved faster compared with the observations (Figs. 5k,l). After 0200 LST 14 October 2011, the atmosphere over Guangdong Province was controlled by dry northerly air, and the frontal rainfall had weakened and moved out across the western Pacific (Figs. 5m–o). Given the analysis above, the results of the numerical simulation of this frontal rainfall event were considered credible.

5. Urban AHF and ULUC influence

As discussed above (see Fig. 3), the center of the distribution of the frontal rainstorm was located over the northeastern PRD (Fig. 6a). The incorporation of AHF caused a sharp increase of over 90 mm in the 24-h accumulated precipitation over the PRD, primarily over the western side of the Pearl River estuary (Fig. 6b), which represents an increase of 6.30% (Table 3). It is indicated that consideration of AHF and ULUC had similar effect in producing increased rainfall over the PRD by affecting surface meteorological variables. However, the incorporation of ULUC enhanced another rainstorm over the eastern side of the Pearl River estuary (Fig. 6c), and it led to a 7.44% increase in

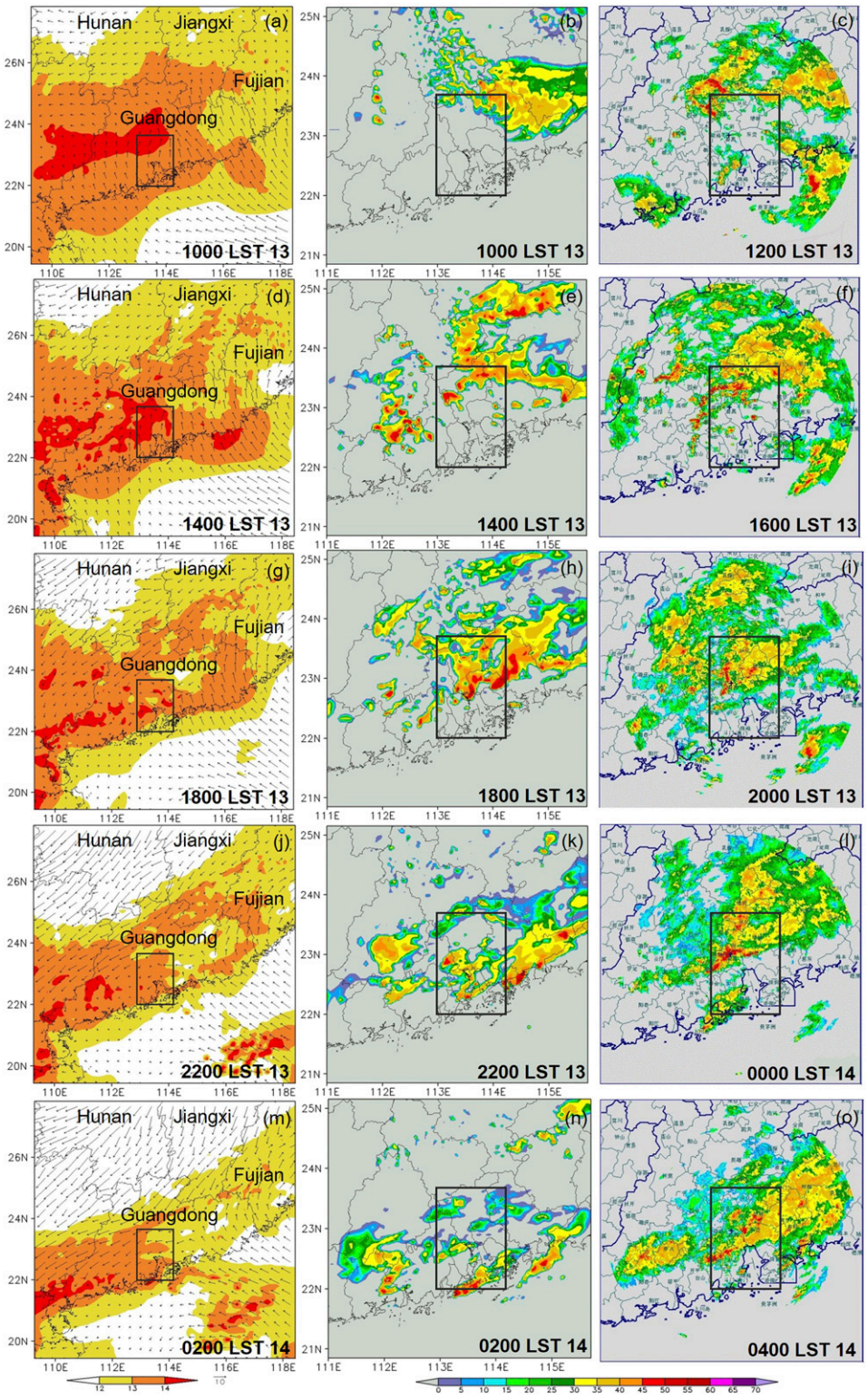

FIG. 5. Simulated water vapor mixing ratio (shading; g kg^{-1}, scale runs from <12 to >14) and wind (vectors; m s^{-1}, vector scale of 10 is under the 116°E longitude at the bottom) at 850 hPa for (a) 1000 LST 13 Oct, (d) 1400 LST 13 Oct, (g) 1800 LST 13 Oct, (j) 2200 LST 13 Oct, and (m) 0200 LST 14 Oct, and simulated and radar-observed (https://nmc.gov.cn/) reflectivity (dBZ, scale runs from <0 to >70) in D03 for (b) 1000 LST 13 Oct, (c) 1200 LST 13 Oct, (e) 1400 LST 13 Oct, (f) 1600 LST 13 Oct, (h) 1800 LST 13 Oct, (i) 2000 LST 13 Oct, (k) 2200 LST 13 Oct, (l) 0000 LST 14 Oct, (n) 0200 LST 14 Oct, and (o) 0400 LST 14 Oct.

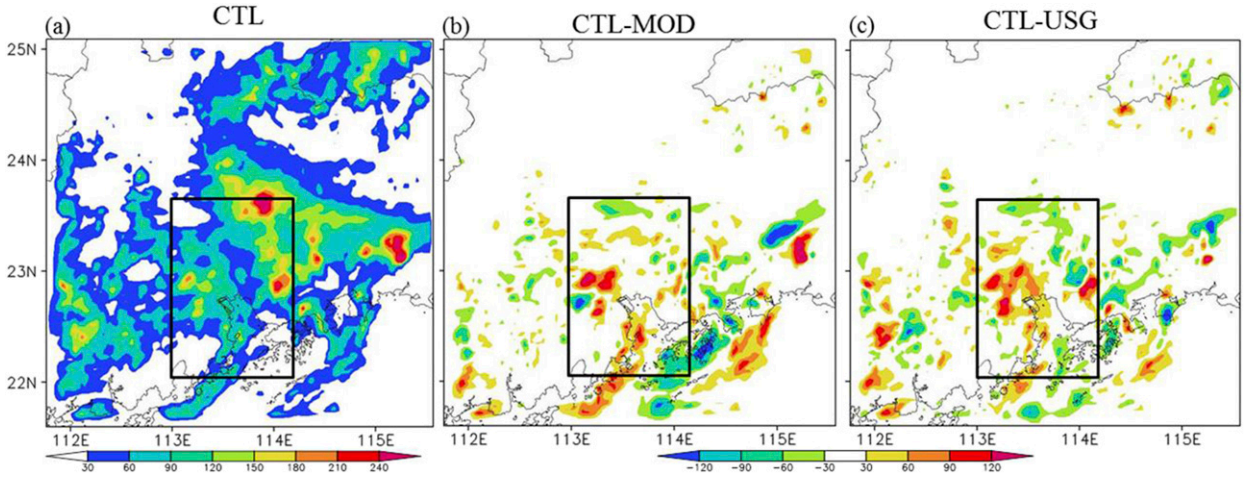

FIG. 6. Simulated 24-h accumulated precipitation (shading; mm) from 0800 LST 13 Oct to 0800 LST 14 Oct 2011 in D03 for (a) CTL (scale goes from <30 to >240 mm), and the difference between (b) CTL and MOD and between (c) CTL and USG [for (b) and (c) the scale goes from <−120 to >120 mm].

accumulated precipitation over the PRD (Table 3). It is evident that the area of increased rainfall when considering AHF and LULC was in reasonable agreement with the observations. However, there was clear distinction in the peak value of the hourly averaged PRD precipitation, although the curves produced by the CTL, MOD, and USG simulations were similar (Fig. 4). Peak values of 8.40, 6.74, and 6.93 mm occurred at 1700 LST for the CTL, MOD, and USG simulations, respectively, equivalent to an increase of 24.63% (comparing MOD with CTL) and 21.21% (comparing USG with CTL), despite the maximum of the MOD simulation at 1900 LST. An explanation for the earlier occurrence of the heavy rainfall in the simulations, in comparison with the observations, might be that the overestimated surface wind in the simulations (Table 2) pushed the cold front southeastward faster, which caused the cold continental air to meet the warm maritime air prematurely.

Incorporation of AHF and ULUC caused the local and even regional meteorological variables to be modified notably, especially surface temperature and humidity. The simulated daily average temperature at 2 m and relative humidity at 2 m (Fig. 7a) show that the surface temperature decreased with increasing latitude, and that there was a UHI effect with warmer temperatures (above 25°C) and an urban dry island (UDI) effect with centers of low humidity (below 90%) in the urban areas. The PRD average 2-m temperature of CTL was closest to the observations with values of 24.13° and 24.19°C, respectively, whereas that of the MOD and

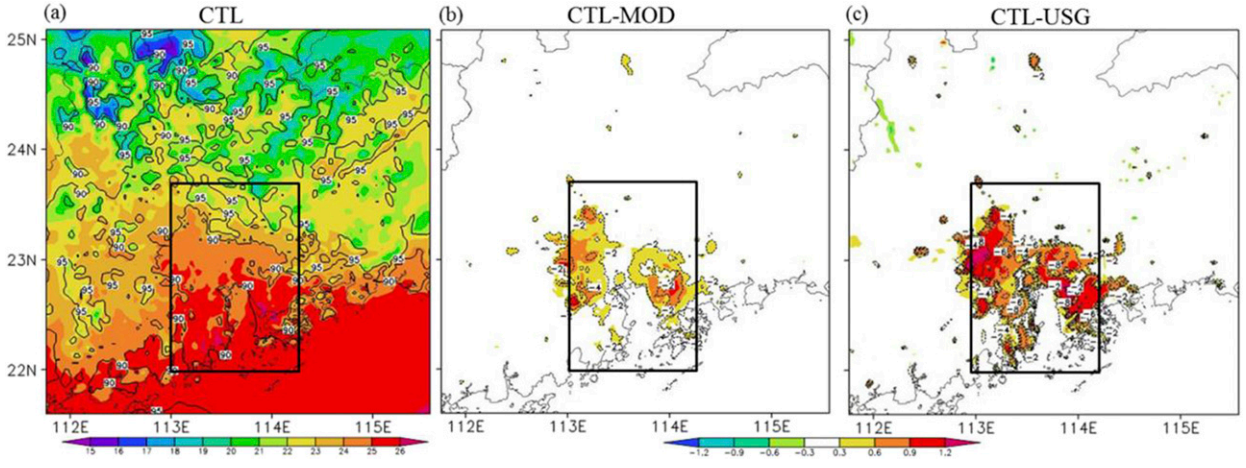

FIG. 7. (a) Simulated daily average 2-m temperature for CTL (shading; °C, with the scale going from <−15 to >26) and 2-m relative humidity (contours; %) from 0800 LST 13 Oct to 0800 LST 14 Oct 2011 in D03, and the difference (b) between CTL and MOD and (c) between CTL and USG for temperature (shading, going from <−1.2° and >1.2°C) and relative humidity (contours).

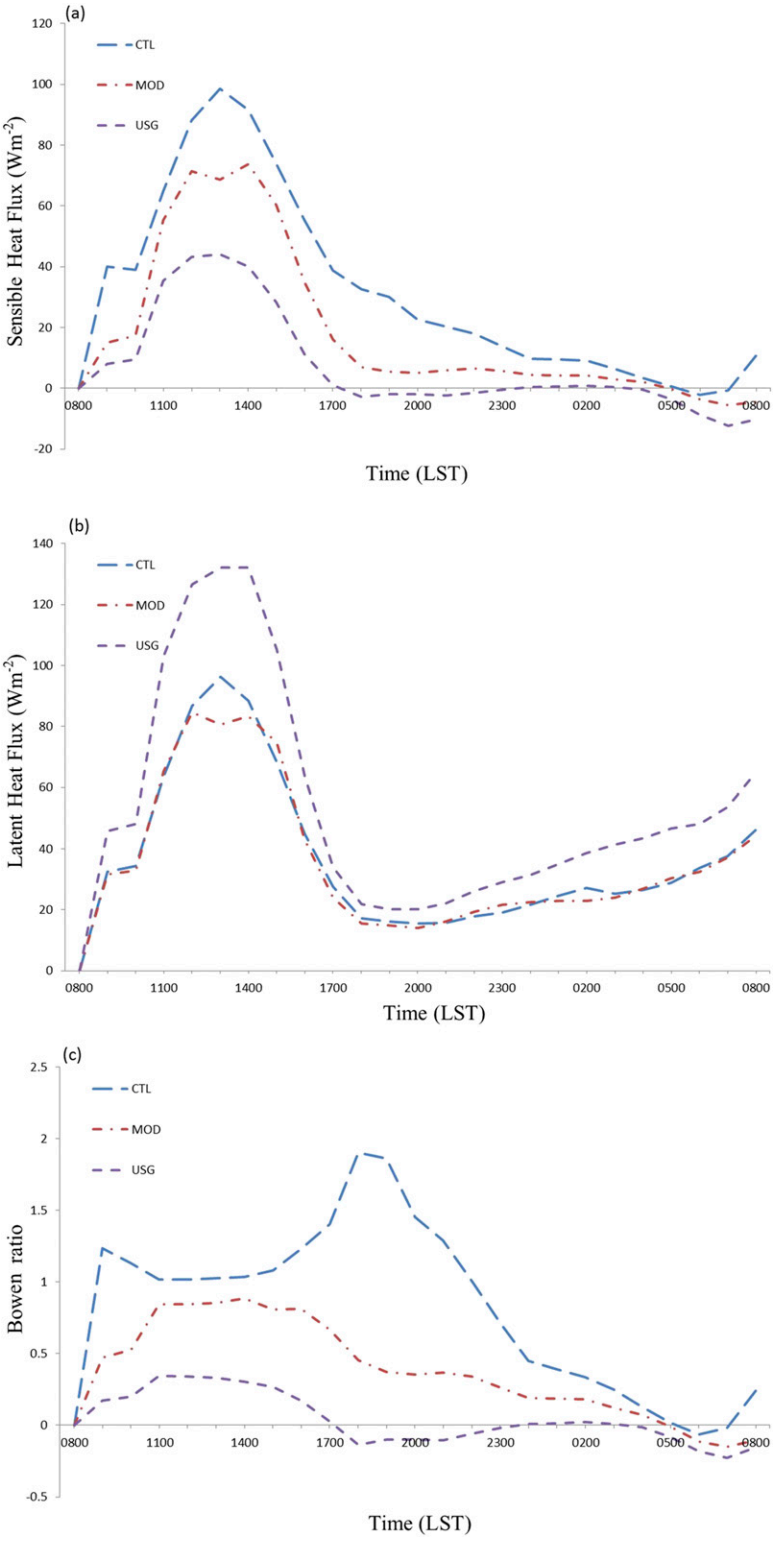

FIG. 8. PRD hourly averaged (a) upward sensible heat flux at the surface, (b) upward latent heat flux, and (c) Bowen ratio at the surface from 0800 LST 13 Oct to 0800 LST 14 Oct 2011.

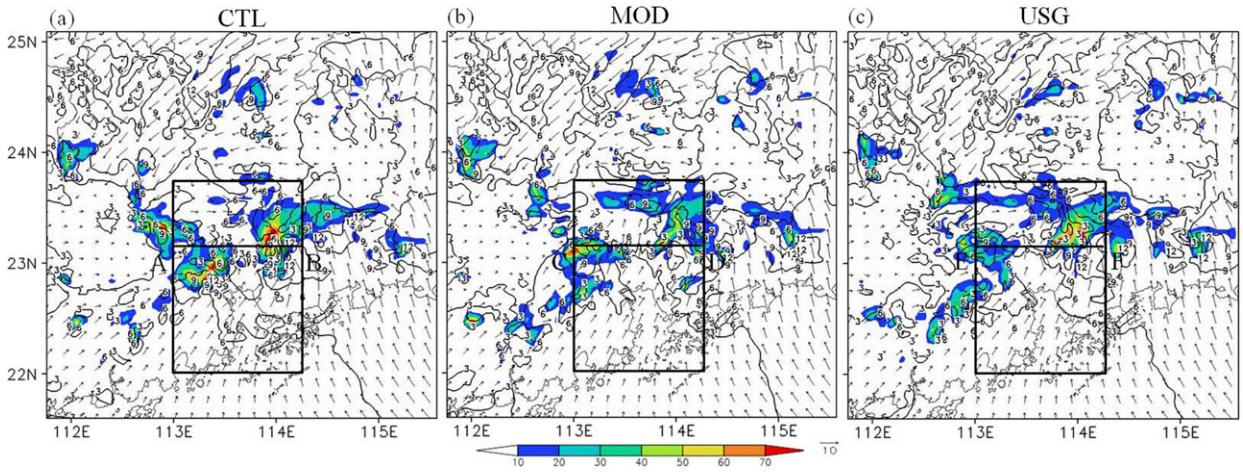

FIG. 9. Simulated precipitation (shading; mm), winds (contours; m s^{-1}) and wind vectors (m s^{-1}) at the 850-hPa level at 1700 LST 13 Oct 2011 in D03 for (a) CTL, (b) MOD, and (c) USG.

USG simulations was 23.94° and 23.80°C, respectively. In the PRD, a moderate difference was found between the CTL and MOD simulations with 2-m temperatures 1°C warmer and 2-m relative humidity 6% lower in the urban areas (Fig. 7b). As for the CTL and USG simulations, the difference over large areas of the PRD was greater than 1.2°C in 2-m temperature and −8% in 2-m relative humidity (Fig. 7c). The maximum differences attributable to the incorporation of AHF and ULUC were 1.46° and 1.44°C in 2-m temperature and 12.51% and 12.79% in 2-m relative humidity, respectively. The similar patterns of distribution of surface temperature and relative humidity were mainly attributable to the urban surface when considering ULUC, because it has comparatively lower albedo and higher capacity for heat capacity from the ground to atmosphere than dry land, cropland, and pasture, whereas consideration of AHF intensifies the UHI and UDI effects directly. As described above, it was evident that the area of increased rainfall in the simulations was in reasonable agreement when considering AHF and ULUC because of the UHI and UDI effects, which are conducive to the convergence of air and the increase of unstable energy in urban areas.

According to previous studies (e.g., Offerle et al. 2005; Sailor 2011), the UHI affects heat flux indirectly through reducing surface reflection and promoting additional shortwave radiation, whereas AHF affects SHF directly. Figures 8a and 8b show that both upward SHF and LHF at the surface increase during daylight and decrease at night, and that the differences attributable to AHF and ULUC are considerable. In the CTL, SHF reached a high value of 98.62 W m^{-2} at 1300 LTS, whereas the maximum in the MOD and USG simulations was comparatively low at 73.76 and 44.06 W m^{-2}, respectively. Furthermore, SHF maintained mostly positive values because of the ULUC, while values over rural surfaces were lower or negative overnight. Because the surface of an urban area has little moisture, upward LHF in the USG was always higher than the MOD and CTL simulations; the maximum difference between the USG and MOD simulations was 51.67 W m^{-2} at 1400 LST. The Bowen ratios (i.e., the ratio of surface SHF to LHF; Bowen 1926) of the CTL, MOD, and USG simulations indicate that because of the incorporation of AHF and ULUC more energy is put into heating the air than evaporating water (Fig. 8c).

It is noted that strong reflectivity occurred along the edge of the LLJ, which implies interaction occurred between the rainfall and the LLJ (e.g., Choi et al. 2011). Figure 9 shows the simulated low-level wind associated with the precipitation at the time of peak rainfall over the PRD (1700 LST 13 October 2011). At 850 hPa, a southwesterly wind dominated over southern Guangdong, and the synoptic-scale LLJ with a region of wind speed greater than 12 m s^{-1} transported abundant water vapor from the South China Sea to the center of the area of maximum hourly rainfall (23.15°N, 113.95°E). For the CTL, the LLJ located to the south of the CTL storm enhanced the precipitation, whereas the LLJ was located to the southeast of the storms in the MOD and USG simulations. Comparison of the CTL and MOD simulations revealed that the AHF enhanced the center of maximum rainfall in the urban areas. Because of the two land-use datasets used in the MOD and USG simulations, another rainstorm developed on the western side of the Pearl River estuary. The differences in the precipitation characteristics and

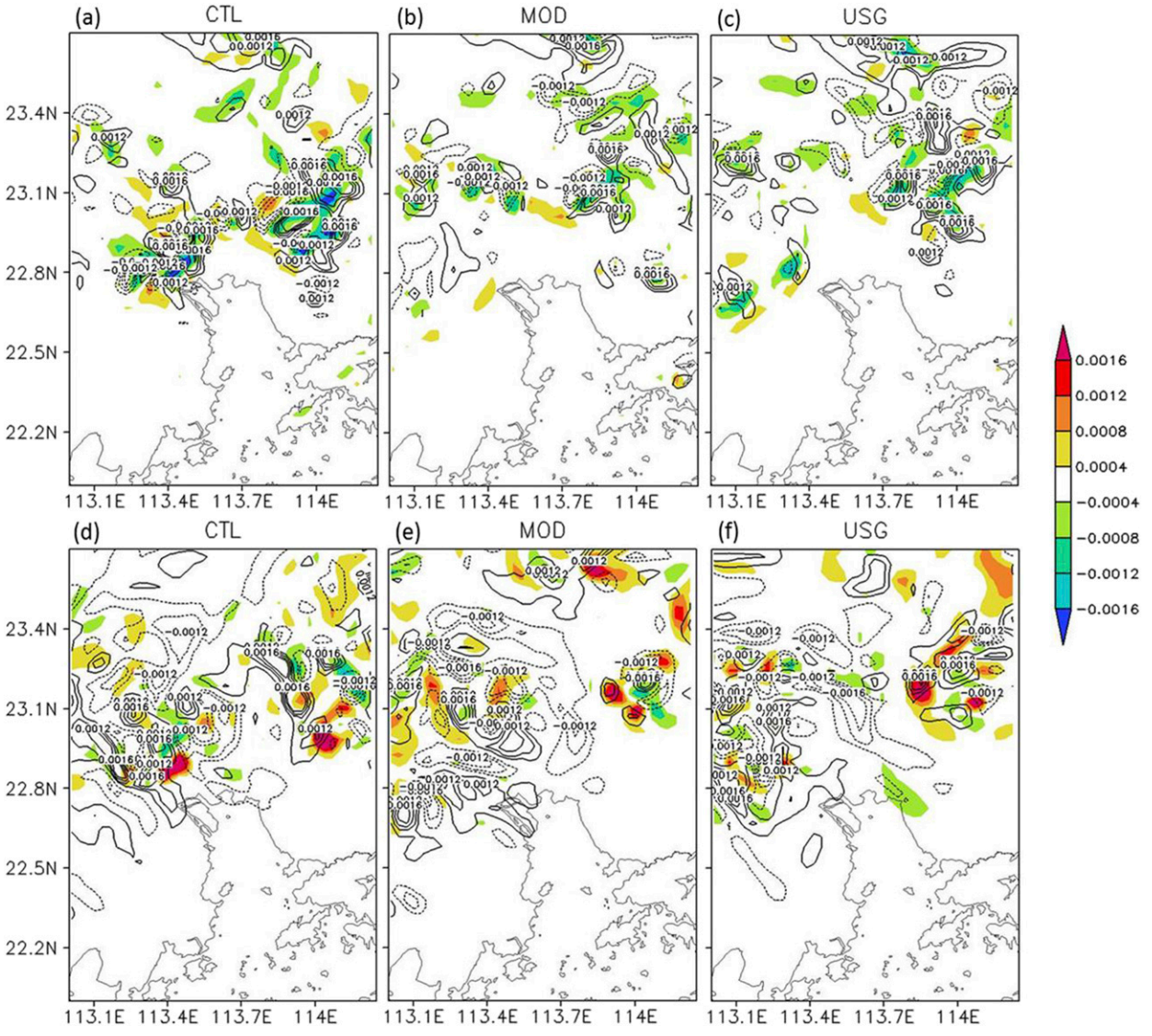

FIG. 10. Simulated divergence (shading; s^{-1}) and vorticity (contours; s^{-1}) at 1700 LST 13 Oct 2011 in the PRD for (a),(d) CTL, (b),(e) MOD, and (c),(f) USG at the (top) 850- and (bottom) 300-hPa levels.

positioning of the LLJ could be explained by building clusters associated with ULUC slowing the cold front and generating suitable initial conditions for the rainstorm, whereas AHF provided more energy for the frontal rainfall of the heavier rainstorm inside the center by strengthening the LLJ.

For the center of the storm in the CTL, two cells of strong convergence appeared over the southeastern portion of the area of heavy precipitation at the lower level, as indicated by large areas of positive vorticity of more than $0.0016\,s^{-1}$ and negative divergence of less than $-0.0016\,s^{-1}$ (Fig. 10a), whereas two cells of divergence occupied the northwestern portion. The same distribution of convergence and divergence also occurred in the MOD (Fig. 10b). As for the USG, only one cell of convergence and one cell of divergence dominated the eastern side of the Pearl River estuary (Fig. 10c). The counter parts of divergence at 300 hPa were roughly opposite (Figs. 10d–f) over the rainstorms. However, positive upper-level vortices occurred in both CTL and USG in contrast to the negative vortices in the MOD, indicating stronger and higher development of the convective cloud clusters.

With regard to the vertical complication within the storms, a longitude–pressure section through the center of the area of maximum precipitation (23.15°N in Fig. 9) is plotted in Fig. 11. The maximum rainfall of the CTL storm was up to 74.62 mm, whereas it was

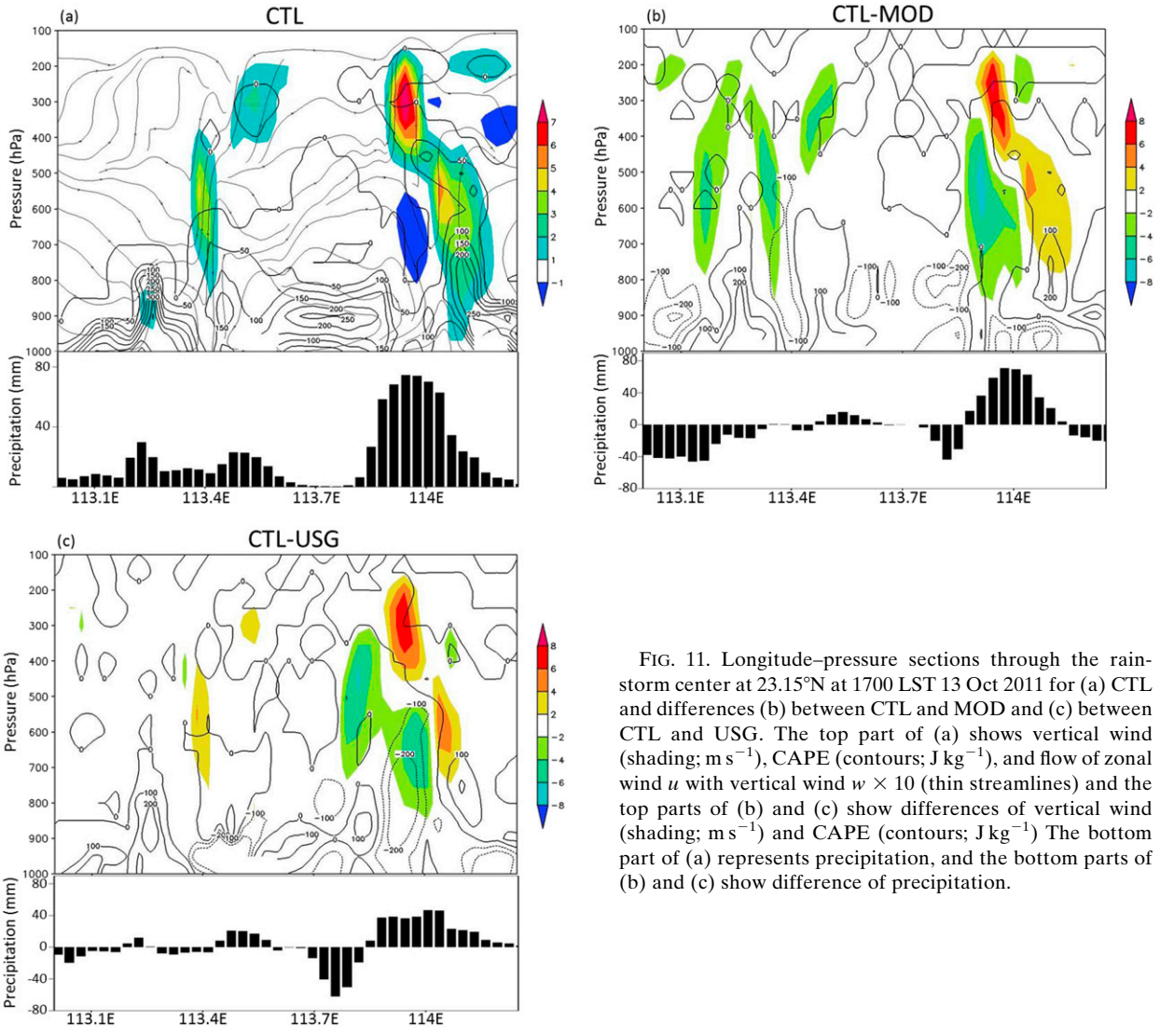

FIG. 11. Longitude–pressure sections through the rainstorm center at 23.15°N at 1700 LST 13 Oct 2011 for (a) CTL and differences (b) between CTL and MOD and (c) between CTL and USG. The top part of (a) shows vertical wind (shading; m s^{-1}), CAPE (contours; J kg^{-1}), and flow of zonal wind u with vertical wind $w \times 10$ (thin streamlines) and the top parts of (b) and (c) show differences of vertical wind (shading; m s^{-1}) and CAPE (contours; J kg^{-1}) The bottom part of (a) represents precipitation, and the bottom parts of (b) and (c) show difference of precipitation.

only 57.36 and 62.43 mm in the MOD and USG simulations, respectively. Strong ascent with maximum speed of more than 7 m s^{-1} was found to reach 300 hPa above the center of maximum rainfall in the CTL storm, while another area of strong vertical motion with speed of 5 m s^{-1} was found around 600 hPa on the eastern side (Fig. 11a). It was also clear that strong downward motion occurred at the center of the convective cell bringing cold dry air from the upper troposphere to the west to surface, which enhanced the convective instability. Apparently, the vertical motion was affected considerably by the distribution of CAPE at mid- and low levels and the maximum CAPE of 200 J kg^{-1} extended to 800 hPa. As discussed above for the MOD, two rainstorms developed simultaneously and the sharp decrease of CAPE at mid- and low levels led to substantial reduction of vertical upward motion through the rainstorm and no downward motion penetrated to the east of the rainfall (Fig. 11b). Consequently, the rainfall was lighter over the eastern storm and heavier in the western storm. For the USG, a moderate–strong rainstorm with decreasing upward motion and CAPE, in comparison with the CTL, and no downward motion led to less precipitation at the rainfall center (Fig. 11c). It might be inferred that AHF and ULUC in producing the UHI and UDI effects enhanced the convective instability via the release of additional CAPE in the middle and low levels. This powerful energy would not only sustain the steady upward motion but it would also create conditions favorable for downward motion, which could have generated a tilted structure

for the rainstorm producing larger convective clouds with longer life-spans and heavier precipitation.

6. Conclusions and future work

A frontal rainfall event that occurred over the PRD on 13–14 October 2011 was studied using the WRF-ARW Model (version 3.3). Synoptic charts and radar-observed reflectivity over southern China were analyzed to investigate the weather conditions that generated the rainstorm. The model predictions, which included surface temperature, humidity, and sea level pressure, were found in good agreement with the observation data obtained from automatic weather stations, although the simulated wind did not match the observations precisely. Furthermore, the second precipitation peak was underestimated, and the model-simulated convection occurred two hours early in comparison with the observed radar data. Generally, the simulation results conformed well to the actual situation, representing the formation, development, and extinction of the frontal rainfall and capturing the distribution of the peak value.

In addition, two experiments using the WRF Model coupled with the UCM were performed to study the impact of AHF and ULUC on the frontal rainfall. Incorporation of AHF caused a sharp increase of over 90 mm in the 24-h accumulated precipitation, primarily in urban areas, which represented an increase of 6.30% in the PRD accumulated precipitation, whereas the incorporation of ULUC caused an increase of 7.44%. In addition, the incorporation of AHF and ULUC caused an increase of the peak value of hourly rainfall rate by 21.21% and 21.04%, respectively. Recent studies based on observations and numerical analyses have shown that the urban environment can play a substantial role in storm evolution and heavy rainfall distribution (e.g., Ntelekos et al. 2008).

To analyze the reasons for the distinct distribution of precipitation, examination of the differences of several key components over the PRD was performed. The simulated results showed that AHF and urban expansion in the PRD caused the simulated daily average surface temperature, upward SHF, and Bowen ratio to increase, whereas the daily average surface relative humidity and upward LHF at the surface were reduced. It was found that urbanization induces an intense UHI effect by supplying additional energy that produces unstable conditions beneficial for generating heavy precipitation, as supported by many previous studies (e.g., Miao et al. 2011).

The lower- and upper-level structures of the simulated mature convective cells were analyzed at the time of peak rainfall. Two strong southward LLJs located over the urban areas carried abundant water vapor to the south of the storm center at 850 hPa. Correspondingly, two strong convective cells appeared at 850 and 300 hPa in the scenario with greater human disturbance, while only one strong rainstorm occurred in the scenario with less human disturbance. The differences in precipitation and convective cell characteristics could be explained by building clusters associated with the ULUC slowing the cold front and generating suitable initial conditions for the rainstorm, whereas AHF provided more energy for the frontal rainfall of the heavier precipitation inside the center by strengthening the LLJ.

The differences in the vertical structure of the rainstorm at the center of the area of maximum precipitation were also investigated. The AHF and ULUC initiated a stronger and more powerful urban rainstorm with greater upward motion from the cloud base to the cloud top and downward motion at the center of the convective cell, which displayed a tilted vertical structure. From the perspective of dynamics, additional CAPE introduced from the urban surface and enhanced by the AHF, released in the middle and low levels, would not only sustain the steady upward motion but also create conditions favorable for downward motion. This could produce larger convective clouds with longer life-spans and heavier precipitation over the PRD.

The studied frontal rainfall event occurred in October because a cold front moved from the northwest toward the southeast and interacted with a warm moist southeasterly wind from the western Pacific Ocean. Such frontal rainfall is different from the thunderstorms that occur in the afternoon in July and August, which are initiated over urban areas and incorporate water vapor collected from the local atmosphere. Thus, the analysis and the derived conclusions regarding the effects of AHF and ULUC in this study might not be applicable to summertime thunderstorm development. However, continued urbanization throughout the world will not only affect frontal rainfall but it will also change the global climate through generating heavier precipitation on the synoptic scale. In future studies, additional cases over larger synoptic scales and longer periods in all seasons should be investigated to produce results that are more robust.

Acknowledgments. The authors were supported by the National Key R&D Program of China (2018YFC1507402), National Natural Science Foundation of China (41875168 and 41705117), and Guangzhou Science and Technology Plan (201707010088). We thank James Buxton, MSc, from Liwen Bianji, Edanz Group China (https://www.liwenbianji.cn./ac), for editing the English text of this paper.

REFERENCES

Alexander, L. V., X. B. Zhang, T. C. Peterson, J. Caesar, and J. L. Vazquez-Aguirre, 2006: Global observed changes in daily climate extremes of temperature and precipitation. *J. Geophys. Res.*, **111**, D05109, https://doi.org/10.1029/2005JD006290.

Allan, R. P., and B. J. Soden, 2008: Atmospheric warming and the amplification of precipitation extremes. *Science*, **321**, 1481–1484, https://doi.org/10.1126/science.1160787.

Allen, L., F. Lindberg, and C. S. B. Grimmond, 2011: Global to city scale urban anthropogenic heat flux: Model and variability. *Int. J. Climatol.*, **31**, 1990–2005, https://doi.org/10.1002/joc.2210.

Ashley, W. S., M. L. Bentley, and J. A. Stallins, 2012: Urban-induced thunderstorm modification in the Southeast United States. *Climatic Change*, **113**, 481–498, https://doi.org/10.1007/s10584-011-0324-1.

Bowen, I. S., 1926: The ratio of heat losses by conduction and by evaporation from any water surface. *Phys. Rev.*, **27**, 779–787, https://doi.org/10.1103/PhysRev.27.779.

Chen, F., and J. Dudhia, 2001: Coupling an advanced land surface–hydrology model with the Penn State–NCAR MM5 modeling system. Part I: Model implementation and sensitivity. *Mon. Wea. Rev.*, **129**, 569–585, https://doi.org/10.1175/1520-0493(2001)129<0569:CAALSH>2.0.CO;2.

Chen, J., Q. Li, J. Niu, and L. Sun, 2011: Regional climate change and local urbanization effects on weather variables in southeast China. *Stochastic Environ. Res. Risk Assess.*, **25**, 555–565, https://doi.org/10.1007/s00477-010-0421-0.

Chen, X., Y. Feng, J. Li, W. Lin, S. Fan, A. Wang, S. Fong, and H. Lin, 2009: Numerical simulations on the effect of sea–land breezes on atmospheric haze over the Pearl River Delta region. *Environ. Model. Assess.*, **14**, 351–363, https://doi.org/10.1007/s10666-007-9131-5.

Chen, Y., and N. Zhang, 2018: Urban heat island mitigation effectiveness under extreme heat conditions in the Suzhou–Wuxi–Changzhou metropolitan area, China. *J. Appl. Meteor. Climatol.*, **57**, 235–253, https://doi.org/10.1175/JAMC-D-17-0101.1.

Cheng, W. Y. Y., and W. J. Steenburgh, 2005: Evaluation of surface sensible weather forecast by the WRF and the Eta Models over the Western United States. *Wea. Forecasting*, **20**, 812–821, https://doi.org/10.1175/WAF885.1.

Ching, J., and Coauthors, 2009: National Urban Database and Access Portal Tool. *Bull. Amer. Meteor. Soc.*, **90**, 1157–1168, https://doi.org/10.1175/2009BAMS2675.1.

Choi, H. Y., J. H. Ha, D. K. Lee, and Y. H. Kuo, 2011: Analysis and simulation of mesoscale convective systems accompanying heavy rainfall: The Goyang case. *Asia-Pac. J. Atmos. Sci.*, **47**, 265–279, https://doi.org/10.1007/s13143-011-0015-x.

Daley, R., 1991: *Atmospheric Data Analysis*. Cambridge University Press, 480 pp.

Dou, J., Y. Wang, R. Bornstein, and S. Miao, 2015: Observed spatial characteristics of Beijing urban climate impacts on summer thunderstorms. *J. Appl. Meteor. Climatol.*, **54**, 94–105, https://doi.org/10.1175/JAMC-D-13-0355.1.

Dudhia, J., 1989: Numerical study of convection observed during the winter monsoon experiment using a mesoscale two-dimensional model. *J. Atmos. Sci.*, **46**, 3077–3107, https://doi.org/10.1175/1520-0469(1989)046<3077:NSOCOD>2.0.CO;2.

Gilliam, R. C., C. Hogrefe, and S. T. Rao, 2006: New methods for evaluating meteorological models used in air quality applications. *Atmos. Environ.*, **40**, 5073–5086, https://doi.org/10.1016/j.atmosenv.2006.01.023.

Giorgi, F., and C. Shields, 1999: Tests of precipitation parameterizations available in latest version of NCAR regional climate model (RegCM) over continental United States. *J. Geophys. Res.*, **104**, 6353–6375, https://doi.org/10.1029/98JD01164.

Grell, G. A., and D. Devenyi, 2002: A generalized approach to parameterizing convection combining ensemble and data assimilation techniques. *Geophys. Res. Lett.*, **29**, 1693, https://doi.org/10.1029/2002GL015311.

Grum, M., A. T. Jorgensen, R. M. Johansen, and J. J. Linde, 2006: The effect of climate change on urban drainage: An evaluation based on regional climate model simulations. *Water Sci. Technol.*, **54**, 9–15, https://doi.org/10.2166/wst.2006.592.

Gutiérrez, E., J. E. Gonzalez, A. Martilli, R. Bornstein, and M. Arend, 2015: Simulations of a heat-wave event in New York City using a multilayer urban parameterization. *J. Appl. Meteor. Climatol.*, **54**, 283–301, https://doi.org/10.1175/JAMC-D-14-0028.1.

Guo, X., D. Fu, and J. Wang, 2006: Mesoscale convective precipitation system modified by urbanization in Beijing City. *Atmos. Res.*, **82**, 112–126, https://doi.org/10.1016/j.atmosres.2005.12.007.

Hand, L. M., and J. M. Shepherd, 2009: An investigation of warm-season spatial rainfall variability in Oklahoma City: Possible linkages to urbanization and prevailing wind. *J. Appl. Meteor. Climatol.*, **48**, 251–269, https://doi.org/10.1175/2008JAMC2036.1.

Hong, S.-Y., and J.-O. J. Lim, 2006: The WRF single-moment 6-class microphysics scheme (WSM6). *J. Korean Meteor. Soc.*, **42**, 129–151, https://www2.mmm.ucar.edu/wrf/users/phys_refs/MICRO_PHYS/WSM6.pdf.

——, and H. L. Pan, 1996: Nonlocal boundary layer vertical diffusion in a medium-range forecast model. *Mon. Wea. Rev.*, **124**, 2322–2339, https://doi.org/10.1175/1520-0493(1996)124<2322:NBLVDI>2.0.CO;2.

James, A. S., M. L. Baeck, A. A. Ntelekos, G. Villarini, and M. Steine, 2011: Extreme rainfall and flooding from orographic thunderstorms in the central Appalachians. *Water Resour. Res.*, **47**, W04514, https://doi.org/10.1029/2010WR010190.

Jin, M. L., R. E. Dickinson, and D. L. Zhang, 2005: The footprint of urban areas on global climate as characterized by MODIS. *J. Climate*, **18**, 1551–1565, https://doi.org/10.1175/JCLI3334.1.

Kaufmann, R. K., K. C. Seto, A. Schneider, Z. T. Liu, L. M. Zhou, and W. L. Wang, 2007: Climate response to rapid urban growth: Evidence of a human-induced precipitation deficit. *J. Climate*, **20**, 2299–2306, https://doi.org/10.1175/JCLI4109.1.

Kusaka, H., and F. Kimura, 2004: Coupling a single-layer urban canopy model with a simple atmospheric model: Impact on urban heat island simulation for an idealized case. *J. Meteor. Soc. Japan*, **82**, 67–80, https://doi.org/10.2151/jmsj.82.67.

——, H. Kondo, Y. Kikegawa, and F. Kimura, 2001: A simple single-layer urban canopymodel for atmospheric models: Comparison with multi-layer and slab models. *Bound.-Layer Meteor.*, **101**, 329–358, https://doi.org/10.1023/A:1019207923078.

Lin, C. Y., F. Chen, J. C. Huang, W. C. Chen, Y. A. Liou, W. N. Chen, and S. C. Liu, 2008: Urban heat island effect and its impact on boundary layer development and land–sea circulation over northern Taiwan. *Atmos. Environ.*, **42**, 5635–5649, https://doi.org/10.1016/j.atmosenv.2008.03.015.

Lin, W., L. Zhang, D. Du, L. Yang, H. Lin, Y. Zhang, and J. Li, 2009: Quantification of land use/land cover changes in Pearl River Delta and its impact on regional climate in summer using numerical modeling. *Reg. Environ. Change*, **9**, 75–82, https://doi.org/10.1007/s10113-008-0057-5.

——, and Coauthors, 2007: A numerical study of the influence of urban expansion on monthly climate in dry autumn over the

Pearl River Delta, China. *Theor. Appl. Climatol.*, **89**, 63–72, https://doi.org/10.1007/s00704-006-0244-6.

Meng, W., H. Li, Y. Zhang, G. Dai, and Q. Wan, 2012: A modeling study of the impacts of Pearl River Delta urban environment on convective precipitation. *Chin. J. Atmos. Sci.*, **36**, 1063–1076.

Miao, S., F. Chen, Q. Li, and S. Fan, 2011: Impacts of urban processes and urbanization on summer precipitation: A case study of heavy rainfall in Beijing on 1 August 2006. *J. Appl. Meteor. Climatol.*, **50**, 806–825, https://doi.org/10.1175/2010JAMC2513.1.

Mlawer, E. J., S. J. Taubman, P. D. Brown, M. J. Iacono, and S. A. Clough, 1997: Radiative transfer for inhomogeneous atmosphere: RRTM, a validated correlated-*k* model for the longwave. *J. Geophys. Res.*, **102**, 16 663–16 682, https://doi.org/10.1029/97JD00237.

Nemunaitis-Berry, K. L., P. M. Klein, J. B. Basara, and E. Fedorovich, 2017: Sensitivity of predictions of the urban surface energy balance and heat island to variations of urban canopy parameters in simulations with the WRF Model. *J. Appl. Meteor. Climatol.*, **56**, 573–595, https://doi.org/10.1175/JAMC-D-16-0157.1.

Nie, W., F. Z. Benjamin, G. Ni, and T. Sun, 2017: Impacts of anthropogenic heat on summertime rainfall in Beijing. *J. Hydrometeor.*, **18**, 693–712, https://doi.org/10.1175/JHM-D-16-0173.1.

Ntelekos, A. A., J. A. Smith, M. L. Baeck, W. F. Krajewski, A. J. Miller, and R. Goska, 2008: Extreme hydrometeorological events and the urban environment: Dissecting the 7 July 2004 thunderstorm over the Baltimore MD metropolitan region. *Water Resour. Res.*, **44**, W08446, https://doi.org/10.1029/2007WR006346.

Offerle, B., C. S. B. Grimmond, and K. Fortuniak, 2005: Heat storage and anthropogenic heat flux in relation to the energy balance of a central European city centre. *Int. J. Climatol.*, **25**, 1405–1419, https://doi.org/10.1002/joc.1198.

Parker, D. E., 2004: Large-scale warming is not urban. *Nature*, **432**, 290, https://doi.org/10.1038/432290a.

——, 2006: A demonstration that large-scale warming is not urban. *J. Climate*, **19**, 2882–2895, https://doi.org/10.1175/JCLI3730.1.

Rontu, L., 2006: A study on parameterization of orography-related momentum fluxes in a synoptic-scale NWP model. *Tellus*, **58A**, 69–81, https://doi.org/10.1111/j.1600-0870.2006.00162.x.

Sailor, D. J., 2011: A review of methods for estimating anthropogenic heat and moisture emissions in the urban environment. *Int. J. Climatol.*, **31**, 189–199, https://doi.org/10.1002/joc.2106.

——, and L. Lu, 2004: A top-down methodology for developing diurnal and seasonal anthropogenic heating profiles for urban areas. *Atmos. Environ.*, **38**, 2737–2748, https://doi.org/10.1016/j.atmosenv.2004.01.034.

——, and M. Hart, 2006: An anthropogenic heating database for major U.S. cities. *Sixth Symp. on the Urban Environment*, Atlanta, GA, Amer. Meteor. Soc., 5.6., https://ams.confex.com/ams/pdfpapers/105377.pdf.

Schmid, P. E., and D. Niyogi, 2017: Modeling urban precipitation modification by spatially heterogeneous aerosols. *J. Appl. Meteor. Climatol.*, **56**, 2141–2153, https://doi.org/10.1175/JAMC-D-16-0320.1.

Shem, W., and M. Shepherd, 2009: On the impact of urbanization on summertime thunderstorms in Atlanta: Two numerical model case studies. *Atmos. Res.*, **92**, 172–189, https://doi.org/10.1016/j.atmosres.2008.09.013.

Shepherd, J. M., H. Pierce, and A. J. Negri, 2002: Rainfall modification by major urban areas: Observations from spaceborne rain radar on the TRMM satellite. *J. Appl. Meteor.*, **41**, 689–701, https://doi.org/10.1175/1520-0450(2002)041<0689:RMBMUA>2.0.CO;2.

Shin, H., and S.-Y. Hong, 2009: Quantitative precipitation forecast experiments of heavy rainfall over Jeju Island on 14-16 September 2007 using the WRF model. *Asia-Pac. J. Atmos. Sci.*, **45**, 71–89.

Skamarock W. C., and Coauthors, 2008. A description of the Advanced Research WRF version 3. NCAR Tech. Note NCAR/TN-475+STR, 113 pp., https://doi.org/10.5065/D68S4MVH.

Wan, Q., and J. Xu, 2011: A numerical study of the rainstorm characteristics of the June 2005 flash flood with WRF/GSI data assimilation system over south-east China. *Hydrol. Processes*, **25**, 1327–1341, https://doi.org/10.1002/hyp.7882.

Wang, W., and N. L. Seaman, 1997: A comparison study of convective parameterization schemes in a mesoscale model. *Mon. Wea. Rev.*, **125**, 252–278, https://doi.org/10.1175/1520-0493(1997)125<0252:ACSOCP>2.0.CO;2.

Wang, Z., and X. Wang, 2011: Estimation and sensitivity test of anthropogenic heat flux in Guangzhou. *J. Meteor. Sci.*, **31**, 422–430.

Yang, P., G. Ren, and W. Hou, 2017: Temporal–spatial patterns of relative humidity and the urban dryness island effect in Beijing city. *J. Appl. Meteor. Climatol.*, **56**, 2221–2237, https://doi.org/10.1175/JAMC-D-16-0338.1.

Zhang C. L., F. Chen, S. G. Miao, Q. C. Li, X. A. Xia, and C. Y. Xuan, 2009: Impacts of urban expansion and future green planting on summer precipitation in the Beijing metropolitan area. *J. Geophys. Res.*, **114**, D02116, https://doi.org/10.1029/2008JD010328.